A Deep Learning Model for Road Damage Detection After an Earthquake Based on Synthetic Aperture Radar (SAR) and Field Datasets

Sadra Karimzadeh [ORCID], Mohammad Ghasemi [ORCID], Masashi Matsuoka [ORCID], Koichi Yagi, and Abdullah Can Zulfikar

Abstract—This article is a new assessment of damaged roads after the Kumamoto earthquake in southern Japan (2016) using remotely sensed synthetic aperture radar (SAR) data, field data and deep learning. Three SAR images from descending orbits of Sentinel-1 in vertical-vertical polarizations are considered for radiometric calibration, geocoding and interferometric analyses. Field data in terms of the international roughness index (IRI) were gathered over more than 530 km using a smartphone accelerometer and the BumpRecorder application. The relationship between SAR data and IRI data was investigated in a binary (0 and 1) mode to establish a multilayer perceptron model of damaged and intact roads. We found the remote sensing SAR datasets suitable, not only for the detection of damaged roads, but also as an indicator of road roughness changes. The classification results for damaged and intact roads indicated that our datasets (SAR and field measurements), together with a deep learning model, yielded acceptable overall accuracy (87.1%).

Index Terms—Deep learning, international roughness index (IRI), Kumamoto, synthetic aperture radar (SAR).

I. INTRODUCTION

TRANSPORTATION infrastructure elements are essential for national development. Intercity transportation networks are vital parts of daily life in populated communities since they facilitate the movement of people, products, and services. Moreover, infrastructure plays a vital role in promoting socioeconomic welfare and sustainability in our world [1], [2]. Road networks are the most substantial forms of transportation infrastructure. Smooth and nonstop performance is highly important for transportation network stability after natural disasters [3].

Earthquakes can occur anywhere worldwide. According to previous experiences, like other infrastructure types, road networks are also at risk, and any failure in their components may result in economic damages and disruptions in relief, rescue, and evacuation activities in the region. Road destruction may limit the movement of emergency vehicles and directly affect rescue and emergency aid actions in the damaged area, resulting in spatial disturbances, increased travel times, and subsequent economic, social, and livelihood losses. Therefore, two of the main goals of disaster management are minimizing disaster effects and formulating efficient emergency plans and risk alleviation strategies [4]. Hence, it is essential to perform injury and loss evaluations following earthquakes and road network damage and the harm to economic growth and social sustainability must be considered [5]. The extensive repairs for failed transportation infrastructure usually take several months or years to complete after an earthquake so that the transportation network will remain disrupted to some extent during the repair period. The timely recovery of an out-of-service transport network is essential because it will improve the efficiency of traffic flows and, more importantly, accelerate long-term attempts to repair other vital infrastructure types [6]. Communication, energy, and water systems highly depend on the transportation system. In addition, disrupted traffic networks during long repair periods may be associated with increased risk of car accidents in certain work areas, and public driver safety may be diminished, including those involved in disaster recovery attempts [7].

There has been a long history of studies focusing on the post-disaster modeling of transportation network performance [8], [9]. Road roughness would be increased by the collapse of roads and significant displacement in roads. Road management and control after an earthquake require accurate and rapid methods for detecting and assessing damage [10], [11]. Traditional road monitoring methods based on road surface visual inspections are costly and time-consuming and can yield unreliable and inconsistent results [12], [13]. Pavement is measured using high-efficiency equipment that detects the road profile, and the obtained data are evaluated based on known global indicators. The international roughness index (IRI) is the most popular index that is globally used to assess pavement roughness. The IRI

Sadra Karimzadeh is with the Department of Remote Sensing and GIS, University of Tabriz, Tabriz 5166616471, Iran, and also with the Architecture and Building Engineering, Tokyo Institute of Technology, Yokohama 226-8502, Japan (e-mail: sadra.karimzadeh@gmail.com).

Mohammad Ghasemi is with the Department of Remote Sensing and GIS, University of Tabriz, Tabriz 5166616471, Iran (e-mail: m.ghasemi1997@gmail.com).

Masashi Matsuoka is with the Architecture and Building Engineering, Tokyo Institute of Technology, Yokohama 226-8502, Japan (e-mail: matsuoka.m.ab@m.titech.ac.jp).

Koichi Yagi is with the BumpRecorder Inc., Tokyo 115-0045, Japan (e-mail: yagi@bumprecorder.com).

Abdullah Can Zulfikar is with the Department of Civil Engineering, Gebze Technical University, 41400 Gebze, Turkey (e-mail: aczulfikar@gtu.edu.tr).

is a statistical indicator of irregularity in the pavement surface [14], [15].

The World Bank proposed some standards in Technical Paper 46 to measure the roughness of roads worldwide [16]. Four classes were defined based on the IRI reliability criterion, and they vary with device calibration requirements and the required user accuracy.

1) Class 1 indicates the highest standards of accuracy for IRI measurement, and it involves a longitudinal profile with 0.5 mm precision in the vertical dimension for measurements.

2) Class 2 includes all methods in which the longitudinal profile is required as the IRI measurement basis.

3) Class 3 includes measurement tools that require mathematical computations. After longitudinal profiles of the road are obtained, a computational method is used to evaluate road roughness. Consequently, some simulations are defined considering characteristics related to roads based on the vertical displacement caused by a standard vehicle, and this approach is called the quarter-car model based on a "golden car," which includes a set of masses, springs, and inertial damping systems that interact with the road in the longitudinal profile. Notably, cumulative vertical motions caused by road irregularities can be measured. The IRI is usually reported in m/km or in/mi units.

4) Class 4 refers to the subjective evaluation of the IRI value, such as via visual inspection. Any system used (directly or indirectly) to assess pavement roughness must be integrated with one GPS receiver with high accuracy to provide accurately located measurements.

Currently, measurement systems for riding assessment (three-axis accelerometers and GPS) are available in modern smartphones, which they have been integrated and improved. Hence, many types of these solutions have been proposed with different approaches worldwide [17]–[19]. In general, an increase in the IRI is associated with an increase in pavement roughness, and IRI = 0 represents smooth pavement. However, semiautomated or automated methods have been created to detect damage to paved roads based on computer vision, image processing algorithms, and terrestrial platforms to reduce the influence of manual measurement subjectivity [20]. However, IRI measurements must be collected over a long time window, and a large database is often needed or analysis. Conversely, remote sensing technology can provide efficient and inexpensive images, such as drone-based, airborne laser scanning-based, and satellite imagery [21]. Because remote sensing tools are efficient, they can be used in alternative methods of IRI assessment to complement traditional measurement techniques. Previous attempts at IRI recovery from remote sensing were highly focused on visual remote sensing data and obtained valuable results [22]. Notably, satellite remote sensing, particularly synthetic aperture radar (SAR) remote sensing, has developed over the past two decades, including in transportation monitoring. The main benefits of these techniques are associated with providing highly dense and frequently updated arrays of data and high accessibility to time series through various archives. With a 1–20 m spatial resolution, 5-6 day temporal revisit period, and comprehensive

spatial coverage, SAR imagery has become extremely valuable for monitoring displacement (at the mm scale) using the interferometry technique (InSAR) [19]. Moreover, SAR can provide moderate-resolution images and efficiently process and manage data; thus, a wide range of transportation network-related factors can be assessed. Many studies have aimed to find a correlation between engineering plans and remote sensing techniques. Recent SAR remote sensing studies have shown that it is possible to monitor major urban elements, such as railroads, bridges, and buildings. Amplitude and phase are the two components of SAR images [23]–[25]. Both components can be used to measure deformation, such as that associated with earthquake damage, volcanic activity, land subsidence, and landslides. The phase information is also used in InSAR methods to extract vertical land displacement information. In previously conducted studies [19], [26]–[28], Suanpaga and Yoshikazu [29] developed a model using L-band radar images from the ALOS/PALSAR sensor of the Japan Aerospace Exploration Agency. They collected information about road roughness (IRI) in Ayutthaya Province, Thailand, and a significant relationship between roughness in radar images and the IRI was observed. Fiorentini *et al.* [30] applied an InSAR technique and IRI measurements through a profilometric laser method. They combined this approach with machine learning algorithms to predict average vertical displacement for a 10-km road. The results indicated a clear association between displacement, the interferometry technique used, and IRI values. Gagliardi *et al.* [31] also conducted a study to assess the applicability of moderate-resolution SAR products in the monitoring of local airport runways and noted the high accuracy of SAR data. Other studies have also been conducted in this area. Karimzadeh and Matsuoka [19] used IRI data and *X*-band SAR images to assess the IRI in Tabriz, Iran, and obtained successful results. Previous studies have shown that artificial intelligence can be widely used to solve various problems, including nonlinear pavement engineering problems [32], [33]. Furthermore, deep learning and machine learning techniques are applied in different innovative fields. IRI measurement has some limitations so remote sensing can complement this method. Many researchers have focused on developing advanced statistical models for IRI prediction by developing powerful computational methods, such as machine learning and deep learning, to predict and evaluate the IRI. Qian *et al.* [34] suggested multiple regression methods for predicting IRI deterioration. Hossain *et al.* [16] used an artificial neural network (ANN) to predict the IRI of simple concrete pavement sections. Yousefzadeh *et al.* [22] discussed road profile estimation using an ANN. Mactutis *et al.* [35] analyzed the association between the IRI, cracking, and grooving in more than 317 observations. These studies' results indicated that such techniques could yield reliable results and reduce the traditional analysis time. Road roughness models have been established to predict IRI parameters in most cases.

Machine and deep learning algorithms can be used to adjust data during the training process, and various variables can be considered. As a result, a certain balance among sample size, the number of inputs, and model complexity can be achieved [36]–[38]. The road monitoring methods explained in this article
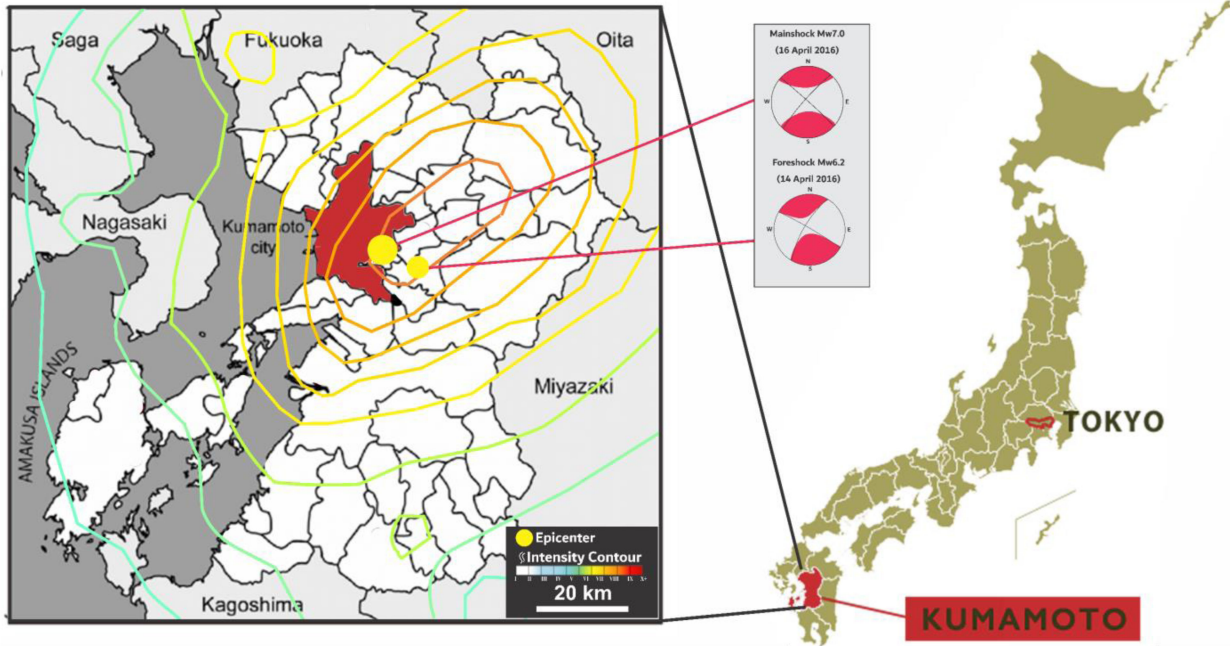
FIGURES

Fig. 1. Modified Mercalli intensity (MMI) map of the M 7.3 Kumamoto earthquake (2016). The yellow circles indicate the locations of the mainshock and preshock.

are taken under different conditions, so the direct comparison of the methods is not appropriate. For example the sensitivity of the *X*-band datasets is higher than the current study (i.e., *C*-band), but the accessibility for X-band data is limited for many areas.

In this article, changes in road roughness after an earthquake in Kumamoto are identified by using remote sensing images as complementary data for IRI analysis. Although both co-polarized (e.g., vertical-vertical) and cross-polarized (e.g., vertical-horizontal) SAR images can be used for this purpose [23]–[25], but here only vertical-vertical (VV) SAR images are selected due to their sensitivity to roughness and confirmed satisfactory qualities in infrastructure monitoring [20]. High spatial-resolution images are discarded due to their high cost and lack of free access, and free images with moderate spatial resolution in the *C*-band are used. Moreover, remote sensing techniques are used, especially radar remote sensing (interferometry). Finally, a deep learning method (multilayer perceptron [MLP]) is applied to predict the IRI using remote sensing parameters.

II. MATERIALS AND METHODS

A. Study Area

Kumamoto city, the capital city of Kumamoto Province, is located in the center of the island of Kyushu at northern latitude 48°32 and eastern longitude 42°103, with an area of 390.32 km^2 (see Fig. 1). According to the census, the population of Kumamoto Province totaled 1 813 000 before the earthquake, and it was reduced to 6000 people six months after the earthquake. Fig. 1 shows the studied area [39].

On 2016/04/14, a magnitude 6.2 earthquake occurred in the region of Kumamoto, Japan. The fault rupture originated from the northern segment of the Hinagu fault. The earthquake caused intense shaking in the eastern part of Kumamoto prefecture and caused major damage in the town of Mashiki near the epicenter. On April 16, 2016, another earthquake, magnitude 7.0 Mw, shook the region. The epicenter of the first shock was reported 12 kilometers northwest of Kumamoto city center, south of Mount Kinpo. The epicenter of the second shock was reported south of Kyushu Prefecture in southwestern Japan. The first shock was called the preshock, and the second shock was called the main shock. The most severe damage occurred in the eastern area of Kumamoto in Mashiki.

The crustal deformation due to the mainshock was observed as ground surface rupture at many locations along the Futagawa fault [40]. These earthquakes have caused significant tangible and intangible damage. The total number of casualties was 1747 [41]. More than 180 000 people were evacuated immediately after the main shock. Total economic losses were estimated at US $ 24 billion to US $ 46 billion [42]. These earthquakes affected several mountainous areas in Kumamoto prefecture, destroying major infrastructure and facilities. In Kumamoto Plain areas, several sections of Kyushu Highway (bridges and cracks in the road surface) were damaged by earthquakes, leading to major disruptions to the regional traffic network. This earthquake killed 55 people and injured more than 3000 others. Many landslides occurred after the earthquake, damaging roads [43], [44]. A mix of IRI information and SAR images were used in this article.

B. Methodology

IRI is a measure of vertical displacement as the horizontal distance traveled along the road [17]. The roughness index is

commonly measured using profilometers, which are devices equipped with sensitive accelerometers or laser sensors that measure the traveled distance and vertical acceleration of the vehicle to which they are attached. In this article, the method of a quarter car (QC) is used which is different from the one-wheel technique that was used a few decades ago. This technique was used using a variety of ordinary cars with a mobile application on the basis of the direct computations of the IRI after removal of effects of the car suspension system. In this article, smartphone and BumpRecorder applications are used. The BumpRecorder application is used to measure vehicle acceleration and the longitudinal profile of the road, and the results are refined based on the vibration frequency [19], [20], [45].

Therefore, the use of this application reduces the need for a driving calibration step. In this article, roughness index measurements obtained before and after the earthquake on major roads and highways in Kumamoto city are used. It is worth noting that the proposed method provides acceptable precision for large projects. The average speed of car movement was 40 km/h, with a measured sampling frequency of 200 Hz. Moreover, each lane of a multilane road was measured to achieve high accuracy. In this article, 28 000 IRIs were collected before the earthquake on July 14, 2013, and 28 000 IRIs were collected after the earthquake on April 20, 2016. The index was measured on both dates by BumpRecorder applications. According to Karimzadeh and Matsuoka [19], the accuracy of the QC method is acceptable for major roads. Still, it may reduce the quality of simultaneous location and acceleration measurements on urban streets, in areas with tall buildings, and in zones of heavy traffic.

For convenience, radar data were compared with the roughness index measurements for system calibration. For all points recorded in the universal transverse mercator (UTM) coordinate system and the radar SAR images in ground coordinates, the radiometric correction was performed based on the roughness index in geographical information system (GIS) software. Then, preprocessed SAR images were input into the proposed method, and all possible points were extracted. Points, including those from GPS receivers, with incorrect coordinates or there were outside the selected range were removed, and the existing cases were revised as needed. The overall study method is shown as a flowchart in Fig. 2.

There are three main steps in the proposed method.
1) Preprocessing for IRI classification.
2) Preprocessing and generation of location change images over time.
3) Deep learning-based forecasting.

This article has generally used two types of information: remote sensing data and IRI data.

Remote sensing techniques are commonly used to extract roads. SAR data can be applied to identify road roughness, and the results can be compared with IRI data; however, road engineers are not familiar with the application of such images. Therefore, remote sensing has not been widely used to assess road roughness. Radar images offer many benefits, such as high sensitivity to physical objects in circadian images rather than optical images, but image complexity can be increased [19], [46].

The sensitivity to roughness is the most important characteristic of SAR images. Moreover, the high location resolution of
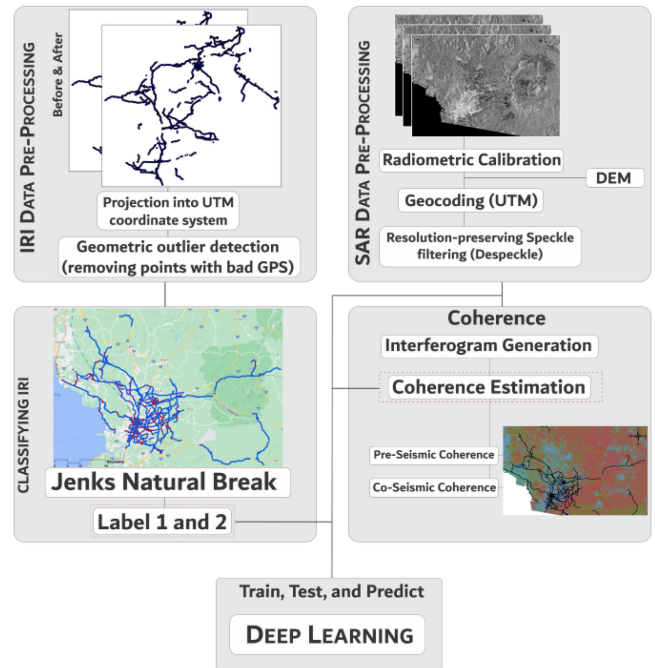

Fig. 2. Workflow of the proposed methodology.

SAR images maximizes the accuracy of classification results. This article focuses on sentinel-1 satellite images from the European Space Agency (ESA) and SAR observations from the sentinel-1 project (two satellites). The sentinel-1 mission began in 2014. This mission combined platforms A and B with a 180° phase difference in a circuit board. Sentinel-1 carries a C-band SAR sensor. This sensor can receive radar images as HH, HV, VV, and VH signals with dual polarization. This mission provides ground images using both sentinel-1 platforms every six days [47], [48].

Here, images from sentinel-1 A in VV polarization were used for comparison with obtain IRI values due to its high backscattering sensitivity to roughness also, two images were used before the earthquake and one image after the earthquake. The incidence angle of the images is 39.4 °and the resolution created from the multilooking procedure is 15 m (azimuth look and range look are 1 and 4, respectively). More information is given in Table I.

Sentinel-1 images were obtained before (two images) and after (one image) the earthquake and used in this article, as given in Table I. Notably, the information in SAR images has high potential for roughness classification commonly used in infrastructure monitoring [19], [24]. However, the detection of damaged and affected roads after an earthquake could be very rapid with such an approach.

As shown in Fig. 2, in this article, we collected two categories of information, one of which is information related to IRI and the other is related to radar images prepared before and after the earthquake. Collected by the BumpRecorder application. The length of the data collection route is 563 km and the same route has been used to collect data after the earthquake. This information was provided by BumpRecorder and provided to our research team. After preprocessing IRI, they were divided

TABLE I
REGISTRATION DATE AND OTHER DETAILS OF SAR IMAGES

Sensor	Date (YYYY/MM/DD)	Polarization	Orbit	Incidence Angle (°)	Resolution
Sentinel-1 A	2016/03/03	VV	Descending	39.4	15m
Sentinel-1 A	2016/03/27	VV	Descending	39.4	15m
Sentinel-1 A	2016/04/20	VV	Descending	39.4	15m

into two categories of good and bad roads, and then the post-earthquake data were divided into two categories: damaged roads and intact roads. Good roads were less scattered before the earthquake and were darker, and bad roads were reversed. In addition, we used the InSAR method to identify changes and to use the deep learning method with the help of SAR and InSAR images; we predicted damaged roads and intact roads. Must be noted, the roads whose IRI values become larger after the earthquake are considered as "damaged roads" in this article.

After data are prepared, data calibration and outlier analysis are key steps for preventing issues with the results. Radar images are characterized by geometric and radiometric errors that must be corrected. IRI data may also include some errors that should be removed. These preprocesses are discussed herein.

SAR images are obtained in the radar coordinate system, which must be converted to a standard ground coordinate system. The radiometric ground correction was applied to eliminate the effects of steep areas on the SAR backscattering values. A digital elevation model (DEM) was used in the conversion process, and a simulated SAR image was produced from the DEM data. In this article, location filters were used to remove noise in images and reduce the noise excitation in images [47]–[49]. Resampling was performed 3×3 windows size. All SAR images were calibrated with a radiometric technique to compare radar brightness and roughness index values.

When preprocessing the statistical IRI data recorded by the application, a different coordinate system is used, and information is stored in a template that is not necessarily suitable for some analyses, such as those that involve GIS applications. The recorded data are also influenced by certain errors. From the high volume of data, incorrect information was identified and excluded from the analysis. If these data were not removed, incorrect results might have been obtained. After this information was removed, the UTM universal coordinate system was selected to allow in-app recall and support different statistical and spatial analyses. SAR images were then preprocessed in one coordinate system. IRI values overlap in some areas of the SAR image. Therefore, we transferred the information for IRI pixels with the same coordinates using GIS techniques [19]. This step was performed for all three images, and the two obtained coherence images were stored in a database.

Fig. 3(a) depicts the pixels extracted from the roughness index information, for which the average backscattering coefficient equaled -7.5 before the earthquake on March 3, 2016, -7.9 (with a standard deviation of 5.09) on March 27, 2016, and -6.48 after the earthquake on April 20, 2016. As seen, the histogram was wider before the earthquake, but became compressed with

higher roughness values after the earthquake. Fig. 3(b) illustrates the pixels in the study area and the backscattering coefficient at decibel values ranging from -77 to 35 before the earthquake and -73 to 37 after the earthquake; these results show a higher backscattering coefficient in areas with brighter pixels and a lower backscattering coefficient in areas with darker pixels. Moreover, Fig. 3(c) indicates the correlation between the backscattering coefficient and the roughness index, which is a partial correlation. Because the radar image was obtained in the *C*-band, the local resolution is moderate, and as the resolution increases, the effects of other phenomena decrease.

Fig. 4 shows the backscattering quantiles for the three radar images. The average values for the initial images on March 3, 2016 and March 27, 2016 equaled -7.548 and -7.98, respectively, and the backscattering value increased to -6.48 after the earthquake, implying an increase in the intensity of backscattering with increased roughness caused by the earthquake. The figure shows that the backscattering range of the images becomes wider after the earthquake.

The radar interferometry technique was used to identify changes in SAR images and indicate visual and spatial changes over time. Spatial changes in SAR images over time were measured based on the estimation of the correlation between the interferometry phases of pairs of images taken before and after the earthquake. The pixel-scale cross-correlation of two SAR image phases at different times before and after the earthquake is called the coherence of the SAR images [43]. To extract a map of spatial changes over time, interferometry values produced by a comparative method were filtered based on the coherence of local scenes and the Goldstein filter [50]. This technique filters areas with large differences from coherent areas to enhance the visualization of deformation margins and reduces the noise levels of temporal and spatial baselines. The coherence technique is valuable in specific applications, such as displacement measurement and the identification of deformation and plate displacement due to earthquakes. As roads are infrastructure components that may change, they are used as forecasting metrics in this article, and radar images are used. The correlation of coherence in the interferometry phase is based on the complex phase values of two SAR acquisition, varies between 0 and 1 and serves as a criterion for evaluating the quality of the generated interferogram. Coherence is defined based on two Gaussian variables *a* and *b*, with a mean value of 0 [51]

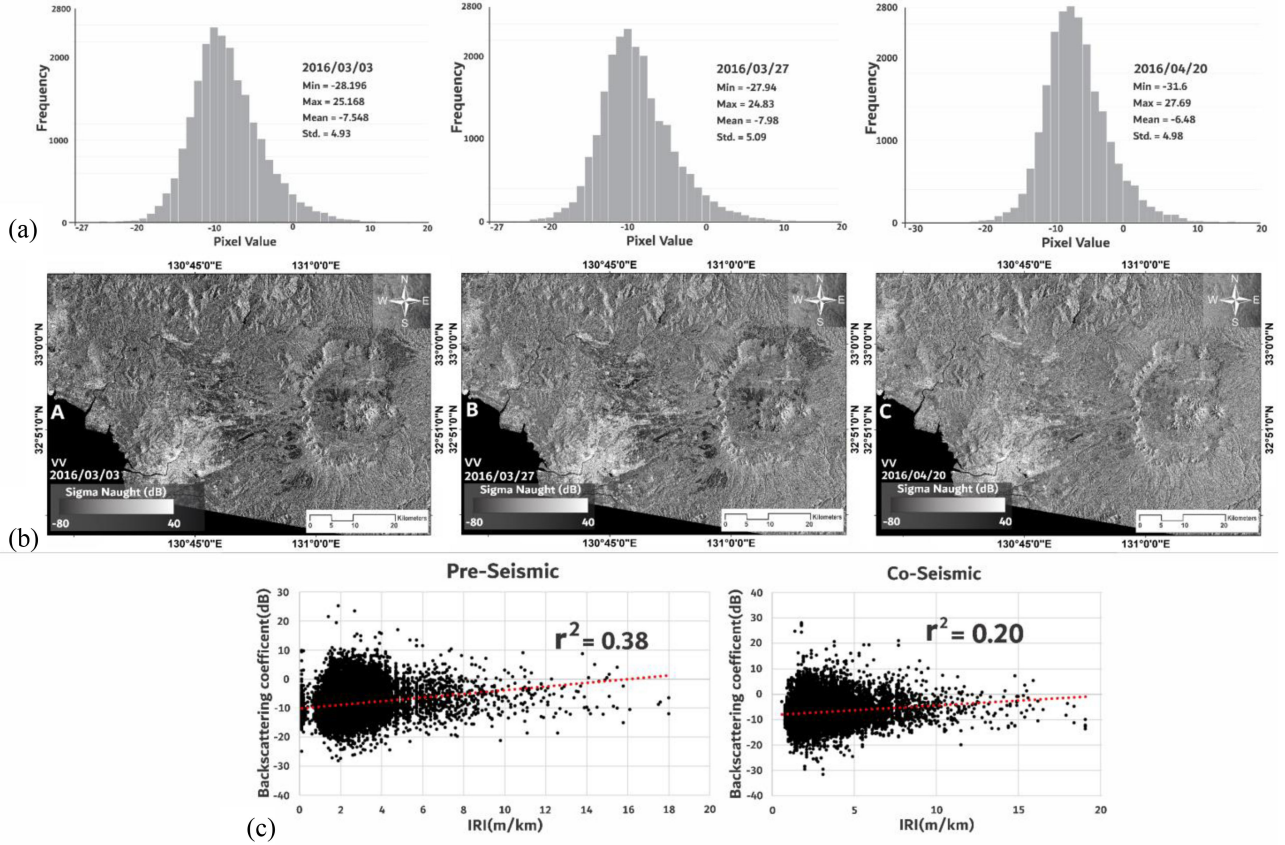$$\gamma = \frac{E(ab^*)}{\sqrt{E(aa^*)E(bb^*)}}. \tag{1}$$

Fig. 3.　(a) Histogram of backscattering in the study area. (b) SAR intensity images used in this article. (c) Scatter plot of IRI measurements and the coefficient of determination (r^2).
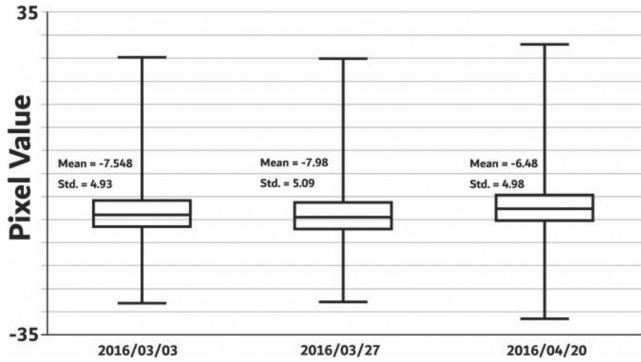

Fig. 4.　Quantiles for the three SAR intensity images.

In (1), a represents the relative integrated value for the original image, and b indicates the relative integrated value for the dependent image. In interferometry analysis, represents a complex image, and E is the expectation operator. In this article, multitemporal analysis was applied to descending datasets (VV polarization) to identify spatial changes in affected areas over time. Additionally, a coherence map was used based on a simple random distinction method [52]

$$\gamma\mathrm{dif} \ = \ \gamma_{\mathrm{pre}} - \gamma_{\mathrm{co}}. \tag{2}$$

The results obtained from (2) can be interpreted as follows: a high coherence value indicates no change over the selected period and vice versa. This method is used to assess changes, but it requires at least three SAR images extracted from a certain path and with a certain geometry. In general, the shorter the distance between images is, the more observable the changes at a small level, such as natural changes and plant growth.

The produced images, including three parameters, were used to illustrate changes as a color composite. The first parameter was forward change, i.e., change related to an event. The second parameter was reverse change, or changes in human activities and vegetation growth. The third parameter was fixed, indicating that no change occurred over the study period. These parameters were designed as follows. After the parameters were calculated, the first, second, and third parameters were assigned to the red, green, and blue channels, respectively [53]

$$\mathrm{Forward} \ = \ \frac{\gamma_{\mathrm{pre}} - \gamma_{\mathrm{post}}}{\gamma_{\mathrm{pre}} + \gamma_{\mathrm{post}}} \tag{3}$$

$$\mathrm{Reverse} \ = \ \frac{\gamma_{\mathrm{post}} - \gamma_{\mathrm{pre}}}{\gamma_{\mathrm{post}} + \gamma_{\mathrm{pre}}} \tag{4}$$

$$\mathrm{Constant} \ = \ \frac{\gamma_{\mathrm{post}} - \gamma_{\mathrm{pre}}}{2}. \tag{5}$$
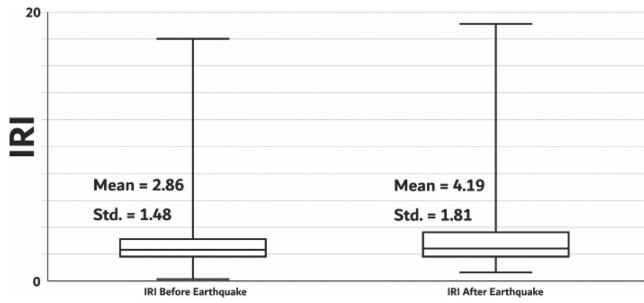
Fig. 5. Distribution of roughness index measurements before and after the earthquake.

Fig. 6. Abstract description of the proposed deep learning process model.

Consequently, the result can be shown as a colored image with three bands that vary in intensity. After the required information was obtained from radar images and coherence information, the road roughness index was classified for forecasting and validation based on IRI values. Therefore, a classification technique was selected, and the available IRI points were divided into training and validation sets to establish and validate the developed IRI mapping algorithm.

C. IRI Classification

In this article, the threshold classification method based on Jenks natural breaks optimization was used due to the lack of information regarding road characteristics and the lack of parameters available to evaluate the IRI forecasting accuracy, before earthquake IRI measurements were used to classify roads into two classes: good and bad. The Jenks natural breaks optimization threshold approach was applied. This method is a data classification technique and was used to determine the ideal classes for IRI values for good and bad roads in this article. Jenks optimization is based on univariate classification, which maximizes the distinction between classes. Thus, this method reduces in-class variance while maximizing inter-category variance [19]. In general, the roads located in the studied area are suitable, except those in a few areas with very poor conditions.

Fig. 5 depicts the distribution of IRI measurements in before and after the earthquake. Before the earthquake, the first and third quartile values were 1.7 and 3.2 m/km, respectively, and after the earthquake, they were 1.9 and 3.8 m/km.

D. Machine Learning

Forecasting or prediction is a process in which a set of inputs is used to estimate the value of an output variable. Machine learning is used in many fields and is commonly applied in conjunction with remote sensing. Machine learning is a branch of artificial intelligence, with a focus on prediction or clustering. In machine learning, the developed algorithms can learn information for modeling. This method can also be used to make predictions. The core step in machine learning includes training based on samples, and two types of information must be selected by the user: inputs based on the data derived from analyses and the output (road roughness here). The algorithm establishes an effective model based on these data, and the model can be used for prediction tasks. In this article, a deep learning technique
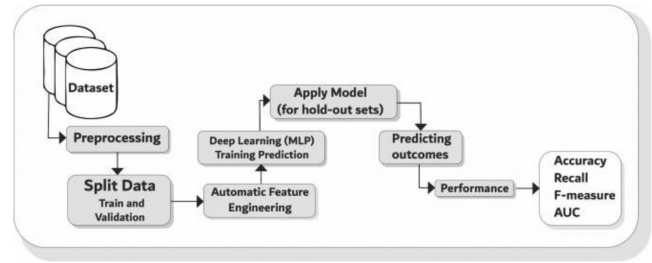
is applied to predict road roughness using remote sensing data [47], [54]–[56].

E. Deep Learning Model

Deep learning is a specific type of machine learning method that uses neural networks, and the deep learning architecture includes several layers. These different layers are used to extract and manipulate features. The output of the previous layer is used as the input of the next layer. Deep learning involves many data conversion and processing steps from the input layer to the output layer. Several hidden layers between the input and output layers allow data from different training layers to be learned. Thus, complex data structures can be identified to adjust parameters in different layers. We suggest a multilayer perceptron (MLP) based binary classifier. Neural networks are used in target recognition and image classification in various fields. To solve complex situations, more layers are needed in a neural network that is fully connected to all neurons, called the MLP neural network [57]. An MLP is a layered network of artificial neurons in which data circulates in one way from the input layer to the output layer, which includes an input layer, an output layer, and hidden layers. The input layer contains network input features. The first hidden layer receives weighted inputs from the input layer and sends the data from the previous layer to the next layer. The output layer contains the classification result. The use of additional layers allows perceptron to solve nonlinear classification problems. Hidden layer neurons use an activation (nonlinear) function. In this article, RapidMiner software was used for optimum MLP design. This software includes a convenient graphic visual environment that supports prediction and classification. The architecture of the algorithm process is shown in Fig. 6. To establish the deep learning model, several steps must be taken: preprocessing and extracting features, producing training and verification datasets, and evaluating model performance. Deep learning has emerged as an important research topic in recent years [58]–[62].

RapidMiner is a data science software platform that provides an integrated environment for data preparation, analysis, and visualization, and it was first published in 2006. This software covers data mining algorithms and supports different neural networks. The software eliminates the need for code writing and relies on operators. Users can link operators without programming knowledge by simply setting parameters for data analysis. Each block includes a set of adjustable parameters related to

TABLE II
MLP PARAMETERS FOR DEEP LEARNING

Parameter	Value	Description
Activation	Rectifier	A rectified linear unit activation function is used in the hidden layers to choose the maximum value of the input.
Hidden layer size	2 layers	The number of hidden layers is limited to only two layers for simplicity and efficiency.
Number of epochs	10.0	The number of iterations performed for the dataset
Epsilon	1.0×10^{-8}	Similar to the learning rate, it promotes forward progress.
Rho	0.99	Rho is the gradient moving average decay factor used for learning rate decay during each update step.
L1	1.0×10^{-5}	A regularization method that constrains the absolute value of the weights is applied
L2	0.0	A regularization method that constrains the sum of the squared weights
Missing value treatment	Mean imputation	Missing values are replaced with the mean value

TABLE III
THRESHOLD OF IRI VALUES FOR GOOD AND BAD ROADS BEFORE THE EARTHQUAKE

Good road	Bad road
IRI < 3.8 m/km	IRI >= 3.8 m/km

a selected algorithm. This software is highly developed and is used in many fields, including remote sensing [63], [64].

Preprocessing includes various substeps, such as role setting and initial transformation. IRI data after the earthquake was processed as ground reference sets and then separated into two categories, namely denoting intact and damaged roads. The after-earthquake roughness value was assigned as 1 and 2, indicating an intact and damaged road, respectively. All data selected for prediction were normalized, and empty records were replaced with suitable values. Then, the data were divided into training and validation sets at a 70/30 ratio. Auto feature engineering is a powerful process in RapidMiner, and a deep learning MLP model is used to internally select a subset of features from a full set of features. The MLP included default parameters that were optimized to find the best set of features. Based on the training dataset, the MLP model was trained to obtain the final features, and optimized default parameter values were obtained with the automodel RapidMiner extension [59].

After the best features were obtained through auto feature engineering, a classification model was used to detect intact and damaged roads. The classification model was a very deep learning MLP model, and it was also used for feature engineering. Table II gives the parameter settings, including the optimized default values, obtained with RapidMiner.

III. RESULTS AND DISCUSSION

In general, acceptable prediction results were obtained with the deep learning algorithm for IRI measurement-SAR data fitting. As mentioned, we classified information with a focus on simple interpretability, and all measurements were classified into two categories using a natural break algorithm. The result suggested that the model could be effectively used to classify roads based on the remote sensing parameters. Fig. 5 depicts the IRI values before and after the earthquake and observable

changes after the earthquake. The thresholds applied in this classification process are given in Table III.

After IRI measurements were classified, we built classification maps to support the required analysis of road roughness before and after the earthquake, as shown in Fig. 7(a) and (b). Road roughness was generally observed in urban areas before the earthquake in Fig. (7a), and major roads were less roughness than smaller roads. In urban areas with many crossroads and traffic routes, the degree of roughness was high. Before the earthquake, road roughness was within an acceptable range, but speed bumps, potholes, and other issues influenced parts of routes. In some cases, routes were initially damaged and became less rough after the earthquake. In such cases, the roughness class was intact and not damaged. However, such areas were rare. In general, high changes were observed after theM7 earthquake, and these changes are shown in Fig. 7. The roughness index increased after the earthquake, as shown in the zoomed black box in Fig. 7(a1)-(2).

Additionally, Fig. 7(b1)-(2) depicts roads with relatively large roughness changes after the earthquake. Notably, the area shown in Fig. 7(b1), with roads passing through farmland zones, experienced great changes. Rationally, the roads around farmlands are less strong than major roads, leading to major post-earthquake changes. Elsewhere, changes were generally minor. Moreover, some crossroads areas changed, perhaps because they were old. In addition, urban roads changed, out-of-town roads generally remained in good condition, and only small roads displayed notable increases in roughness.

Moreover, low roughness values do not necessarily suggest that no change in roughness occurred; in many cases, roads remained intact with only minor changes that did not influence the road class. For example, on section of road had an initial roughness index of 0.4, which reached 1.6 after the earthquake, but this change was not sufficient for the roading being classified as damaged. Some roads displayed initial roughness index values of 3.2 and were classified as intact, but this value increased to 4.1 after the earthquake, leading to a "damaged" classification. However, most roads remained intact after the earthquake, and only rough routes were severely influenced. Major roads experienced fewer changes than side streets for various reasons, such as enhanced construction, more thorough road maintenance, stronger substructures, and other factors.

According to the identified results for each part of the road, the cumulative percentage of IRI values was calculated before and after the earthquake. Fig. 8 illustrates the statistical results for roads before and after the earthquake. Notably, as roads became displaced after the earthquake, the plot shifted to the right. The IRI rates of roads reflect an ascending road roughness trend. The roughness rate equaled 0.1 before the earthquake but reached 0.8 after the disaster; additionally, the density was
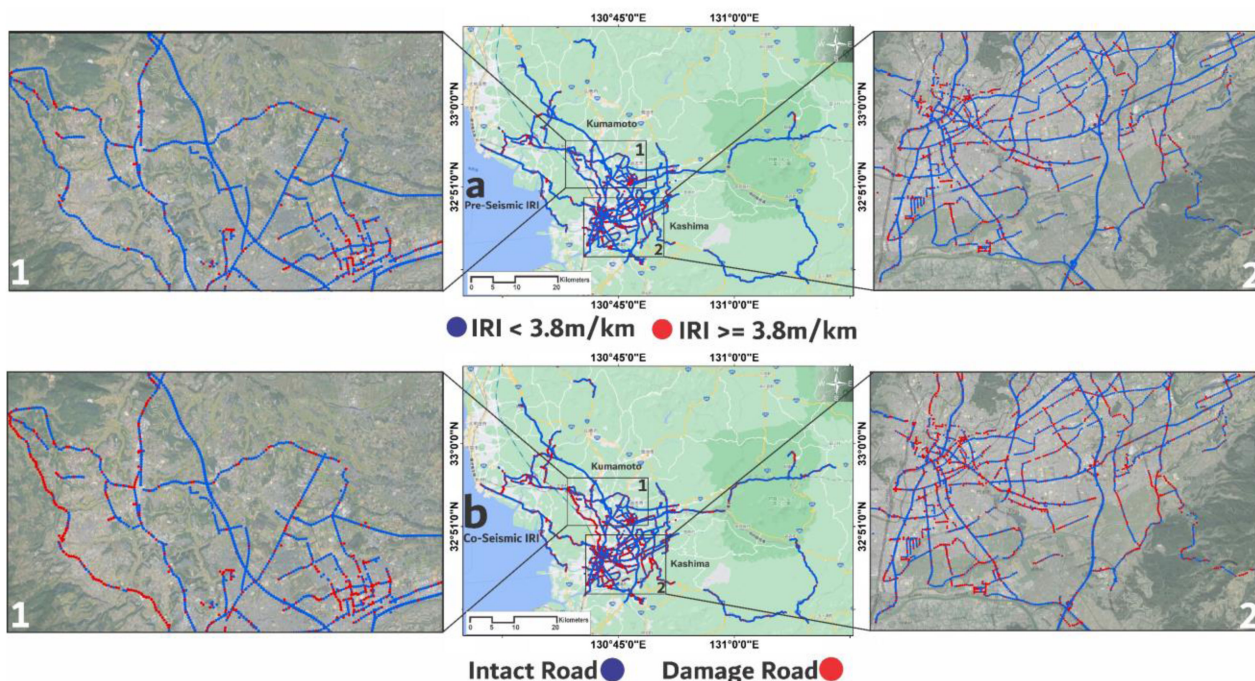
Fig. 7. Natural break classification results for intact roads (blue dots) and damaged roads (red dots) based on the IRI. (a) Before the earthquake. (b) After the earthquake.
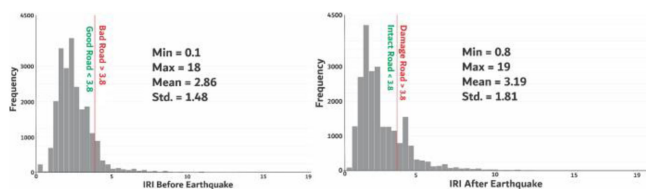

Fig. 8. Statistical results for roughness values before and after the earthquake.

Fig. 9. SAR image-based RGB color combination to visualize changes to roads in the study area.

approximately 1.5–2.5 before the earthquake and 1.9–2.3 after. Changes were also observed for intact roads, but these were not considered since these roads were assigned to class 2. The roughness of intact roads also increased, but classifying these roads as damaged yielded inaccurate results. The closer the IRI value is to zero, the smoother the road is, and vice versa. Among the 28 000 roads for which IRI values were obtained, 24 013 roads were good, and 3987 roads were bad. These values changed to 21 515 intact and 6485 damaged roads after the earthquake. Accordingly, 15% of all roads needed repair before the earthquake, and this rate increased to 25% after the disaster. After the information was classified in text form, the relevant software was used for statistical analysis, and the data were input into the software and labeled to classify and predict the results.

As mentioned, five remote sensing parameters were used in this article, and three preprocessed images were obtained (two initial images before the earthquake and one final image after the earthquake); all three images displayed no polarization distortion. Although dual-polarized or full polarimetric images can provide us more detailed information [66]–[69], but here only VV polarization was used due to its acceptable performance in tasks involving road roughness identification [20], [65]. Two
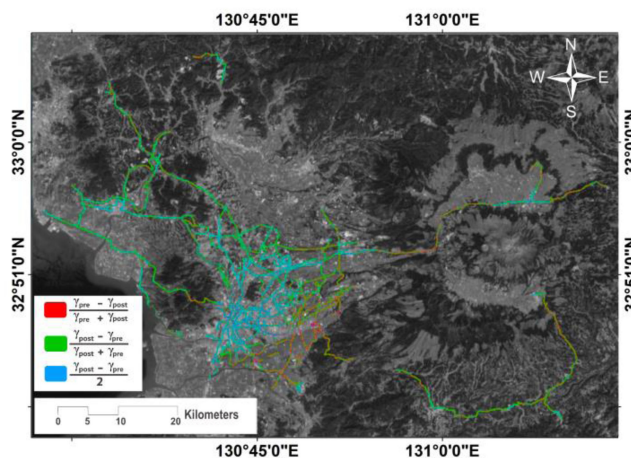
coherence images obtained from the above-described images were used to detect changes. The damage results were predicted using remote sensing data and a deep learning model. The findings are reported herein.

Fig. 9 depicts a colored coherence image composite that indicates changes, with red pixels denoting extensive changes. Southern areas were close to the earthquake epicenter, where changes are clear. Interurban roads of low quality experienced the greatest changes caused by the earthquake. Green areas mainly indicate changes in vegetation. Plants grew, and backscattering highly changed within temporal distance between images. In areas with out-of-town roads and farmland areas, considerable changes were observed in the density of
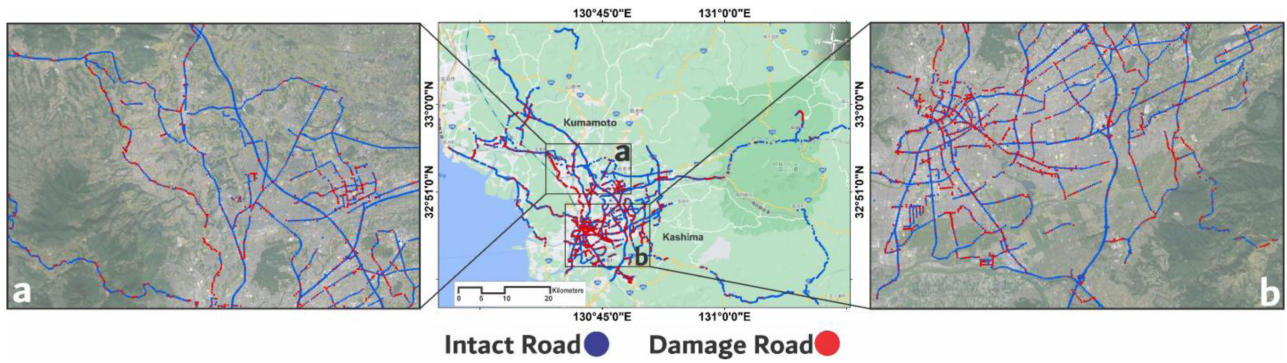
Fig. 10.   Results of road damage prediction based on the proposed deep learning method.

TABLE IV
CONFUSION MATRIX OF THE PROPOSED MODEL

	True range 2	True range 1	Class precision
Pred. range 2	1286	268	82.77%
Pred. range 1	1487	10577	87.67%
Class recall	46.40%	97.53%	

TABLE V
CLASSIFICATION PERFORMANCE OF THE PROPOSED MODEL

ACC (%)	Recall (%)	AUC (%)	F-Measure (%)
87.1%	97.5%	97.5%	83.1%

backscattering. Blue pixels indicate small changes. The results are visually consistent with the measured IRI values, suggesting that the model provides effective predictions.

In this article, the five mentioned remote sensing parameters were input into the deep learning model for prediction. As noted, the studied roads were divided into two classes. The applied algorithm was used to predict changes after the earthquake using training samples. A confusion matrix was used to evaluate algorithm performance; this matrix indicates the relationship between actual and predicted values. Additionally, class precision reflects the performance and accuracy of the algorithm, class recall represents the percentage of classes correctly predicted (%), and accuracy indicates the percentage of correctly predicted based on observations (%), which is the most important criterion used to assess a classification technique. This criterion measures the overall accuracy of classification. The recall(x) criterion represents the precision of class x classification considering all records labeled x. The precision(x) criterion indicates the precision of classification of x for all cases in which the x label was predicted in classification for the considered record. Note that recall(x) indicates the efficiency of classification based on the number of class x occurrences, and precision(x) is related to the prediction precision of classification, indicating to what extent the classification output is reliable.

Moreover, in classification cases in which some records are labeled as undetermined, the denominator of the recall(x) calculation must be considered equal to the total number of records with label x. F-measure(x) is a combination of the recall and precision criteria. This metric is used when it is not possible to consider specific importance for either of these two criteria separately. Area under the curve (AUC) represents the rate of correct prediction, and the closer the AUC is to 100, the higher the prediction precision. The numerical value of AUC is a numerical resolution between 1 and 100 and indicates the power of detection or accuracy of test results. The accuracy of

the test results depends on how well the test method is able show the correct positive and negative results. If this number is close to 100, it means that the data are generally above the bisector line and the positive rate is high, and the test method has good detection or accuracy. This matrix is a useful tool for analyzing the performance of a prediction method when different data, observations, or classes are considered. In the ideal case, the majority of observation data fall along the main diagonal, and the remaining values are zero or close to zero. Accordingly, the prediction results are given in Tables IV and V.

Deep learning was used to analyze the obtained results and produce a binary map. In Fig. 10, the same areas in the images illustrated in Fig. 8 are magnified. The deep learning algorithm displayed relatively high-quality performance. The predicted changes were similar to the changes in the IRI, but there were some incorrect predictions. Such changes are likely related to the use of moderate-resolution images with features in multiple pixels. In addition, the studied area is a humid region with extensive vegetation, so trees and their leaves that grew during the study period negatively affected the backscattering data collection. In particular, areas where interurban roads pass through farmland zones and gardens, as shown in Fig. 10, or with trees growing near roads and highways are often where incorrect predictions occur. In general, the areas close to the earthquake epicenter experienced changes in both coherence and SAR images. The obtained results of the applied algorithm are consistent with observations, indicating the good performance of the approach based on SAR images. As given in Table IV, two classes were designed for prediction using remote sensing parameters and the measured reference IRIs. Classes 1 and 2 indicate intact and damaged roads, respectively. Because the classifications results for class 2 roads were based on all roads in the study area and damaged roads were less common than intact roads, the classification precision was lower for damaged roads than for intact roads. Although the learning model was limited in some cases, 82.77% of the results were acceptable.

Notably, precision was generally higher for intact roads, with more iterations considered. These roads could be assessed under different conditions, and model performance was acceptable.

The precision of predictions for the intact road class equaled 87.67%. According to Table V, the overall precision of the proposed algorithm reached 87.1%, which was an acceptable rate. The AUC indicated the probability of correct precision and equaled 97.5, reflecting the high potential of the proposed algorithm for new data prediction. Moreover, the recall and F-measure values equaled 97.5% and 83.1%, respectively. We found that *C*-band SAR data and coherence can serve as a valuable bases to predict RI values at the road network level and identify and rank roads in need of pavement maintenance and repair. This method can be applied in crisis management and road monitoring. Application of this strategy can accelerate road work and the identification of rough roads, especially if there is a lack of financial resources.

It should be noted that the relationship between the IRI and SAR images may vary in different cases based on the interferometry process of the satellite at a moderate-spatial-resolution power; images with higher spatial resolutions could enhance model performance if considered in other cases. Therefore, the results derived from moderate-resolution images and the proposed deep learning algorithm can be used to effectively evaluate vertical displacement in road networks.

Moreover, various issues may be encountered when identifying changes in roads based on high-resolution images. As given in Table V, the overall precision of the proposed algorithm equaled 87.1%, which indicated good performance. The results of this article were similar to those of Karimzadeh and Matsuoka [19] using SAR images in the *X*- band for the Tabriz-Iran highway, they were able to show the relationship between backscattering and roughness index and Mayer *et al.* [24] using SAR images in *X*-band and roughness index for Virginia showed that there is a relationship between roughness index and SAR data scatter and based on the designed classification, achieved an overall accuracy of 92.6%, who used SAR images for IRI detection. However, in this article, high-accuracy *C*-band images were obtained with the proposed deep learning method.

IV. CONCLUSION

Collecting IRI data with traditional methods is a costly and time-consuming process; therefore, it is difficult to use this technique in practical crisis management and road monitoring. In contrast, remote sensing provides high potential for such tasks, and SAR can provide timely information about local changes in road surface conditions and large volumes of road data in a short amount of time. Therefore, the use of remote sensing parameters to identify road roughness was explored in this article, and a new machine learning method based on deep learning was proposed. The roughness of intact and damaged roads was accurately predicted based on IRI information before and after an earthquake using deep learning and remote sensing techniques. The precision of the proposed method reached 87, suggesting that this approach can be used during crises to rapidly collect data and identify critical areas. In this research, IRI values were obtained using the quarter-car model and a smartphone connected to the car, and *C*-band SAR images with a moderate resolution were used. IRI values were considered references. Although SAR images have some limitations, such as those related to the type of backscattering, they provided high precision overall. The use of satellite-based SAR image for road roughness assessment could minimize the data collection time and promote the establishment of large road quality datasets. Further studies will use the same method and images with higher resolutions to explore other aspects of road roughness classification based on remote sensing data.

REFERENCES

[1] E. Ivanová and J. Masárová, "Importance of road infrastructure in the economic development and competitiveness," *Econ. Manag.*, vol. 18, no. 2, pp. 263–274, Aug. 2013.

[2] N. L. Vandycke, J. M. C. B. Viegas, and J. M. Sarriera, *Global Roadmap of Action Toward Sustainable Mobility*. Washington, DC, USA: World Bank, 2019.

[3] Y. Zhou, S. Banerjee, and M. Shinozuka, "Socio-economic effect of seismic retrofit of bridges for highway transportation networks: A pilot study," *Struct. Infrastructure Eng.*, vol. 6, no. 1/2, pp. 145–157, Feb. 2010.

[4] S. Karimzadeh, M. Miyajima, B. Kamel, and V. Pessina, "A fast topographic characterization of seismic station locations in Iran through integrated use of digital elevation models and GIS," *J. Seismol.*, vol. 19, no. 4, pp. 949–967, Jul. 2015.

[5] K. Kawashima and I. Buckle, "Structural performance of bridges in the Tohoku-Oki earthquake," *Earthq. Spectra*, vol. 29, pp. 315–338, Mar. 2013.

[6] F. Yi and Y. Tu, "An evaluation of the paired assistance to disaster-affected areas program in disaster recovery: The case of the wenchuan earthquake," *Sustainability*, vol. 10, no. 12, Nov. 2018, Art. no. 4483.

[7] H. Yang, K. Ozbay, O. Ozturk, and K. Xie, "Work zone safety analysis and modeling: A state-of-the-art review," *Traffic Inj. Prevention*, vol. 16, no. 4, pp. 387–396, Dec. 2014.

[8] M. Zamanifar and S. M. Seyedhoseyni, "Recovery planning model for roadways network after natural hazards," *Natural Hazards*, vol. 87, no. 2, pp. 699–716, Feb. 2017.

[9] W. Sun, P. Bocchini, and B. D. Davison, "Resilience metrics and measurement methods for transportation infrastructure: The state of the art," *Sustain. Resilient Infrastructure*, vol. 5, no. 3, pp. 168–199, Apr. 2020.

[10] M. Bordoni *et al.*, "Estimation of the susceptibility of a road network to shallow landslides with the integration of the sediment connectivity," *Natural Hazards Earth Syst. Sci.*, vol. 18, no. 6, pp. 1735–1758, Jun. 2018.

[11] O. Mavrouli *et al.*, "Integrated risk assessment due to slope instabilities in the roadway network of gipuzkoa, basque country," *Natural Hazards Earth Syst. Sci.*, vol. 19, no. 2, pp. 399–419, Feb. 2019.

[12] W. Wang *et al.*, "Pavement crack image acquisition methods and crack extraction algorithms: A review," (in English), *J. Traffic Transp. Eng.*, vol. 6, no. 6, pp. 535–556, Dec. 2019.

[13] A. Ragnoli, M. De Blasiis, and A. Di Benedetto, "Pavement distress detection methods: A review," *Infrastructures*, vol. 3, no. 4, Dec. 2018.

[14] L. Inzerillo, G. Di Mino, and R. Roberts, "Image-based 3D reconstruction using traditional and UAV datasets for analysis of road pavement distress," *Autom. Construction*, vol. 96, pp. 457–469, Dec. 2018.

[15] J. Li, Z. Zhang, and W. Wang, "International roughness index and a new solution for its calculation," *J. Transp. Eng. Part B Pavements*, vol. 144, no. 2, Jun. 2018, Art. no. 06018002.

[16] M. I. Hossain, L. S. P. Gopisetti, and M. S. Miah, "International roughness index prediction of flexible pavements using neural networks," *J. Transp. Eng. Part B Pavements*, vol. 145, no. 1, Mar. 2019, Art. no. 04018058.

[17] M. W. Sayers, *Guidelines For Conducting and Calibrating Road Roughness Measurements*. Ann Arbor, MI, USA: Univ. Michigan, 1986.

[18] M. W. Sayers, *The Little Book of Profiling: Basic Information About Measuring and Interpreting Road Profiles*. Ann Arbor, MI, USA: Univ. Michigan, 1998.

[19] S. Karimzadeh and M. Matsuoka, "Remote sensing X-band SAR data for land subsidence and pavement monitoring," *Sensors*, vol. 20, no. 17, Jun. 2020, Art. no. 4751.

[20] S. Karimzadeh and M. Matsuoka, "Development of nationwide road quality map: Remote sensing meets field sensing," *Sensors*, vol. 21, no. 6, Jun. 2021, Art. no. 2251.

[21] D. R. Palamara, M. Nicholson, P. Flentje, E. Baafi, and G. M. Brassington, "An evaluation of airborne laser scan data for coalmine subsidence mapping," *Int. J. Remote Sens.*, vol. 28, no. 15, pp. 3181–3203, Jul. 2007.

[22] M. Yousefzadeh, S. Azadi, and A. Soltani, "Road profile estimation using neural network algorithm," *J. Mech. Sci. Technol.*, vol. 24, no. 3, pp. 743–754, Mar. 2010.

[23] S. Pettinato, E. Santi, S. Paloscia, P. Pampaloni, and G. Fontanelli, "The intercomparison of X-band SAR images from COSMOSkyMed and TerraSAR-X satellites: Case studies," *Remote Sens.*, vol. 5, no. 6, pp. 2928–2942, Jun. 2013.

[24] F. J. Meyer, O. A. Ajadi, and E. J. Hoppe, "Studying the applicability of X-band SAR data to the network-scale mapping of pavement roughness on US roads," *Remote Sens.*, vol. 12, no. 9, May 2020, Art. no. 1507.

[25] O. Ajadi, F. Meyer, and P. Webley, "Change detection in synthetic aperture radar images using a multiscale-driven approach," *Remote Sens.*, vol. 8, no. 6, Jun. 2016, Art. no. 482.

[26] D. Small, L. Zuberbühler, A. Schubert, and E. Meier, "Terrain-flattened gamma nought radarsat-2 backscatter," *Can. J. Remote Sens.*, vol. 37, no. 5, pp. 493–499, Jan. 2011.

[27] M. Lazecky, I. Hlavacova, M. Bakon, J. J. Sousa, D. Perissin, and G. Patricio, "Bridge displacements monitoring using space-borne X-band SAR interferometry," *IEEE J. Sel. Topics Appl. Earth Observ. Remote Sens.*, vol. 10, no. 1, pp. 205–210, Jan. 2017, doi: 10.1109/jstars.2016.2587778.

[28] P. Oliver, C. Samson, and S. Kenny, "Systematic preparation and processing of interferometric synthetic aperture radar data for monitoring linear transportation infrastructure," *J. Appl. Remote Sens.*, vol. 13, no. 2, Apr. 2019, Art. no. 024504.

[29] W. Suanpaga and K. Yoshikazu, "Riding quality model for asphalt pavement monitoring using phase array type L-band synthetic aperture radar (PALSAR)," *Remote Sens.*, vol. 2, no. 11, pp. 2531–2546, Nov. 2010.

[30] N. Fiorentini, M. Maboudi, P. Leandri, and M. Losa, "Can machine learning and PS-InSAR reliably stand in for road profilometric surveys?," *Sensors*, vol. 21, no. 10, Jun. 2021, Art. no. 3377.

[31] V. Gagliardi *et al.*, "Testing sentinel-1 SAR interferometry data for airport runway monitoring: A geostatistical analysis," *Sensors*, vol. 21, no. 17, Jan. 2021, Art. no. 5769.

[32] H. Ceylan, K. Gopalakrishnan, and M. B. Bayrak, "Neural networks based concrete airfield pavement layer moduli backcalculation," *Civil Eng. Environ. Syst.*, vol. 25, no. 3, pp. 185–199, Sep. 2008.

[33] J. R. Saura, F. Debasa, and A. Reyes-Menendez, "Does user generated content characterize millennials' generation behavior? Discussing the relation between SNS and open innovation," *J. Open Innov. Technol. Market Complexity*, vol. 5, no. 4, Nov. 2019.

[34] J. Qian *et al.*, "International roughness index prediction model for thin hot mix asphalt overlay treatment of flexible pavements," *Transp. Res. Rec.*, vol. 2672, no. 40, pp. 7–13, Dec. 2018.

[35] J. A. Mactutis, S. H. Alavi, and W. C. Ott, "Investigation of relationship between roughness and pavement surface distress based on westrack project," *Transp. Res. Rec. J. Transp. Res. Board*, vol. 1699, no. 1, pp. 107–113, Jan. 2000.

[36] J. R. Saura, A. Reyes-Menendez, and F. Filipe, "Comparing data-driven methods for extracting knowledge from user generated content," *J. Open Innov. Technol. Market Complexity*, vol. 5, no. 4, Sep. 2019.

[37] S. Choi and M. Do, "Development of the road pavement deterioration model based on the deep learning method," *Electronics*, vol. 9, no. 1, Dec. 2019.

[38] P. Marcelino, M. de Lurdes Antunes, E. Fortunato, and M. C. Gomes, "Machine learning approach for pavement performance prediction," *Int. J. Pavement Eng.*, vol. 22, no. 3, pp. 341–354, May 2019.

[39] Y. Sasabuchi, H. Matsui, K. Kotani, A. K. Lefor, and H. Yasunaga, "Effect of the 2016 kumamoto earthquakes on preventable hospital admissions: A retrospective cohort study in Japan," *BMJ Open*, vol. 8, no. 7, Jun. 2018, Art. no. e021294.

[40] Fire and Disaster Management Agency. 2016. [Online]. Available: http://www.fdma.go.jp/bn/2016/

[41] Cabinet Office of Government of Japan 2016. "Estimated economic impact due to the 2016 kumamoto earthquakes," 2016, [Online]. Available: http://www5.cao.go.jp/keizai3/kumamotoshisan/kumamotoshisan20160523.pdf, Accessed: Jun. 9, 2016.

[42] K. Okumura, "Earthquake geology of the april 14 and 16, 2016 kumamoto earthquakes," 2016, [Online]. Available: http://home.hiroshima-u.ac.jp/kojiok/kumamoto2016KOreport2.pdf, Accessed: May 15, 2021.

[43] M. Hajeb, S. Karimzadeh, and M. Matsuoka, "SAR and LIDAR datasets for building damage evaluation based on support vector machine and random forest algorithms—A case study of kumamoto earthquake, Japan," *Appl. Sci.*, vol. 10, no. 24, Dec. 2020, Art. no. 8932.

[44] F. Yamazaki, Y. Sagawa, and W. Liu, "Extraction of landslides in the 2016 kumamoto earthquake using multi-temporal lidar data," in *Proc. Earth Resour. Environ. Remote Sens. GIS Appl. IX*, Sep. 2018.

[45] K. Yagi, "Response type roughness measurement and cracking detection method by using smartphone," in *Pavement and Asset Management*. Boca Raton, FL, USA: CRC Press, 2019, pp. 815–822.

[46] W. Emery, A. Yerasi, and N. Longbotham, and F. Pacifici, "Fully automated road network extraction from high-resolution satellite multispectral imagery," in *Proc. IEEE Int. Geosci. Remote Sens. Symp.*, 2014, pp. 1–4.

[47] M. Ghasemi, S. Karimzadeh, and B. Feizizadeh, "Urban classification using preserved information of high dimensional textural features of sentinel-1 images in tabriz, Iran," *Earth Sci. Inform.*, vol. 14, no. 4, pp. 1745–1762, Apr. 2021.

[48] M. Lazecky, F. Canaslan Comut, Y. Qin, and D. Perissin, "Sentinel-1 interferometry system in the high-performance computing environment," in *Lecture Notes in Geoinformation and Cartography*. New York, NY, USA: Springer, 2016, pp. 131–139.

[49] R. Touzi, "A review of speckle filtering in the context of estimation theory," *IEEE Trans. Geosci. Remote Sens.*, vol. 40, no. 11, pp. 2392–2404, Nov. 2002, doi: 10.1109/tgrs.2002.803727.

[50] R. M. Goldstein and C. L. Werner, "Radar interferogram filtering for geophysical applications," *Geophys. Res. Lett.*, vol. 25, no. 21, pp. 4035–4038, Jan. 1998, doi: 10.1029/1998gl900033.

[51] S. Karimzadeh, S. Samsonov, and M. Matsuoka, "Block-based damage assessment of the 2012 ahar-varzaghan, Iran, earthquake through SAR remote senisng data," in *Proc. IEEE Int. Geosci. Remote Sens. Symp.*, 2017, pp. 1546–1549.

[52] M. Hasanlou, R. Shah-Hosseini, S. T. Seydi, S. Karimzadeh, and M. Matsuoka, "Earthquake damage region detection by multitemporal coherence map analysis of radar and multispectral imagery," *Remote Sens.*, vol. 13, no. 6, Mar. 2021, Art. no. 1195.

[53] S. Karimzadeh and M. Matsuoka, "Building damage characterization for the 2016 amatrice earthquake using ascending–descending COSMO-SkyMed data and topographic position index," *IEEE J. Sel. Topics Appl. Earth Observ. Remote Sens.*, vol. 11, no. 8, pp. 2668–2682, Aug. 2018, doi: 10.1109/jstars.2018.2825399.

[54] M. Hajeb, S. Karimzadeh, and A. Fallahi, "Seismic damage assessment in sarpole-zahab town (Iran) using synthetic aperture radar (SAR) images and texture analysis," *Natural Hazards*, vol. 103, no. 1, pp. 347–366, May 2020.

[55] S. Karimzadeh, M. Matsuoka, J. Kuang, and L. Ge, "Spatial prediction of aftershocks triggered by a major earthquake: A binary machine learning perspective," *ISPRS Int. J. Geo-Inf.*, vol. 8, no. 10, Sep. 2019, Art. no. 462.

[56] H.-L. Nguyen *et al.*, "Development of hybrid artificial intelligence approaches and a support vector machine algorithm for predicting the marshall parameters of stone matrix asphalt," *Appl. Sci.*, vol. 9, no. 15, Aug. 2019, Art. no. 3172.

[57] L. Zhang, L. Zhang, and B. Du, "Deep learning for remote sensing data: A technical tutorial on the state of the art," *IEEE Geosci. Remote Sens. Mag.*, vol. 4, no. 2, pp. 22–40, Jun. 2016, doi: 10.1109/MGRS.2016.2540798.

[58] H. Majidifard, Y. Adu-Gyamfi, and W. G. Buttlar, "Deep machine learning approach to develop a new asphalt pavement condition index," *Construction Building Mater.*, vol. 247, Jun. 2020, Art. no. 118513.

[59] M. A. S. Santos, E. D. Assad, A. C. Gurgel, and N. Omar, " Similarity metrics enforcement in seasonal agriculture areas classification," *Remote Sens.*, vol. 12, no. 11, Jun. 2020, Art. no. 1791.

[60] A. Sharma, S. N. Sachdeva, and P. Aggarwal, "Predicting IRI using machine learning techniques," *Int. J. Pavement Res. Technol.*, pp. 1–10, Sep. 2021.

[61] A. Sarker, D. Mollá, and C. Paris, "Automatic evidence quality prediction to support evidence-based decision making," *Artif. Intell. Med.*, vol. 64, no. 2, pp. 89–103, Jun. 2015.

[62] M. Afzal, M. Hussain, R. B. Haynes, and S. Lee, "Context-aware grading of quality evidences for evidence-based decision-making," *Health Inform. J.*, vol. 25, no. 2, pp. 429–445, Aug. 2019.

[63] K. Konstantinos, "Implementation of a web-based platform for data analysis, visualization and machine learning," M.S. Thesis, Data Sci., Int. Hellenic Univ., Thessaloniki, Greece, 2020.

[64] A. Candel and L. Erin, *Deep Learning with H2O*. Mountain View, CA, USA: H2O.ai, 2018.

[65] F. Ulaby and D. Long, *Microwave Radar and Radiometric Remote Sensing*. Ann Arbor, MI, USA: Univ. Michigan, 2015.

[66] S. Chen, X. Wang, and M. Sato, "Urban damage level mapping based on scattering mechanism investigation using fully polarimetric SAR data for the 3.11 east Japan earthquake," *IEEE Trans. Geosci. Remote Sens.*, vol. 54, no. 12, pp. 6919–6929, Dec. 2016, doi: 10.1109/TGRS.2016.2588325.

[67] Y. Ji, J. T. S. Sumantyo, M. Y. Chua, and M. M. Waqar, "Earthquake/Tsunami damage level mapping of urban areas using full polarimetric SAR data," *IEEE J. Sel. Topics Appl. Earth Observ. Remote Sens.*, vol. 11, no. 7, pp. 2296–2309, Jul. 2018, doi: 10.1109/JSTARS.2018.2822825.

[68] S.-E. Park and Y. T. Jung, "Detection of earthquake-induced building damages using polarimetric SAR data," *Remote Sens.*, vol. 12, 2020, Art. no. 137.

[69] E. Ferrentino, F. Nunziata, C. Bignami, L. Graziani, A. Maramai, and M. Migliaccio, "Multi-polarization C-band SAR imagery to quantify damage levels due to the central Italy earthquake," *Int. J. Remote Sens.*, vol. 42, no. 15, pp. 5969–5984, 2021.

Masashi Matsuoka received the B.S. degree in architectural engineering from the Muroran Institute of Technology, Muroran, Japan, in 1990, and the M.S. and Ph.D. degrees from the Tokyo Institute of Technology (Tokyo Tech), Tokyo, Japan, in 1992 and 1996, respectively.

He is currently a Professor with the Department of Architecture and Building Engineering, Tokyo Tech. He was with Tokyo Tech, Remote Sensing Technology Center of Japan, Earthquake Disaster Mitigation Research Center, Kobe, and the National Institute of Advanced Industrial Science and Technology, Tsukuba, prior to returning to Tokyo Tech. He is a Member of the Earthquake Engineering Research Institute and the Architectural Institute of Japan. His current research interests include earthquake engineering, geomorphology, GIS, and application of remote sensing technology to disaster management.

Dr. Matsuoka is a Member of the Earthquake Engineering Research Institute, Tokyo, Japan and the Architectural Institute of Japan, Tokyo, Japan.

Sadra Karimzadeh received the Ph.D. degree in engineering with a certificate of commendation from Kanazawa University, Kanazawa, Japan, in 2015.

He was a Postdoctoral Researcher with the Department of Geographical Information System (GIS) and Remote Sensing, University of Tabriz, Tabriz, Iran, in 2016. From 2016 to 2018, he was a JSPS Researcher with the Department of Architecture and Building Engineering, Tokyo Institute of Technology, Tokyo, Japan. From January 2019 and July 2019, he was a researcher with Geoinformatics Unit, RIKEN,Wak, in Japan. He is currently an Assistant Professor with the Department of GIS and Remote Sensing, University of Tabriz, Tabriz, Iran. His research interests include SAR interferometry, radar imagery for earthquake damage assessment, infrastructure monitoring using SAR, GIS applications for disaster management, and seismic site characterizations based on GIS and remote sensing technologies.

Dr. Karimzadeh is a Reviewer for most of the international journals in remote sensing and earthquake engineering.

Koichi Yagi is currently the Chief Executive Officer of BumpRecorder Co., Ltd., Tokyo, Japan.

Mohammad Ghasemi received the B.S. degree in geography and urban planning and the M.Sc. degree in geographic information system (GIS) from the University of Tabriz, Tabriz, Iran, in 2018 and 2021, respectively.

He is a Member of the Remote Sensing Laboratory University of Tabriz, University of Tabriz. His current research interests include earthquake, SAR interferometry, Web GIS, GIS applications for disaster management, and the application of remote sensing technology to disaster management.

Abdullah Can Zulfikar received the M.Sc. and Ph.D. degrees in civil or earthquake engineering.

He is currently a Civil Engineer and is currently with Civil Engineering Department, Gebze Technical University, Darca, Turkey. His research interests include seismic hazard, risk assessment, earthquake risk reduction technologies, such as near-real-time damage/risk assessment, and early warning systems.